DFT Exploration of Active Site Motifs in Methane Hydroxylation by Ni-ZSM-5 Zeolite

SCHOLARONE™
Manuscripts

Catalysis Science & Technology

ARTICLE

DFT Exploration of Active Site Motifs in Methane Hydroxylation by Ni-ZSM-5 Zeolite†

Muhammad Haris Mahyuddin[a] and Kazunari Yoshizawa*[a]

The O_2-activated Ni-ZSM-5 zeolite is a promising catalyst for the selective oxidation (hydroxylation) of methane to methanol. While UV-vis spectra analyses (Shan et al. *Langmuir* 2014, **30**, 8558–8569) have proposed a bent mono(μ-oxo)dinickel $[Ni_2(\mu\text{-}O)]^{2+}$ as the active site in Ni-ZSM-5, calculations based on density functional theory (DFT) have shown that methane activation on such an active site motif leads to a very high activation barrier, which makes the reaction impossible to proceed at low temperature (<200 °C). Thus, explorations of other possible motifs of Ni active site in ZSM-5 zeolite are indispensable. In the present study, we employed DFT+U method to calculate methane hydroxylation on various motifs of Ni-oxo active species, including $[NiO]^{2+}$, $[Ni_2(\mu\text{-}O)]^{2+}$, $[Ni_2(\mu\text{-}O)_2]^{2+}$, and $[Ni_3(\mu\text{-}O)_3]^{2+}$, in the periodic structure of ZSM-5 zeolite. On the basis of agreement between the previously reported experimental and presently calculated activation energies, we suggest the $[Ni_2(\mu\text{-}O)_2]^{2+}$ and $[Ni_3(\mu\text{-}O)_3]^{2+}$ motifs as two possible candidates for the actual structure of active sites in Ni-ZSM-5. Different from $[Cu_2(\mu\text{-}O)]^{2+}$-exchanged zeolites extensively studied in recent years, the $[Ni_2(\mu\text{-}O)_2]^{2+}$- and $[Ni_3(\mu\text{-}O)_3]^{2+}$-ZSM-5 are predicted to activate methane and desorb the formed methanol with low activation and desorption energies, providing a new direction for the low-temperature methane hydroxylation with spontaneous methanol desorption.

1. Introduction

The direct conversion of methane to methanol is an important reaction as methane is abundant and methanol has enormous potentials as an energy carrier and for chemical feedstock. However, this process remains quite challenging, due to the difficulties in cleaving the strong C–H bonds of methane and preventing the complete oxidation to CO_2. Nature has shown that the iron-containing[1–3] and copper-containing[4–6] methane monooxygenases (MMOs) are able to oxidize methane to methanol at ambient conditions. Inspired by these enzymes, researchers have developed metal-exchanged zeolite catalysts, which have well-defined metal active sites evenly distributed in the crystal lattice and mimic the high activity of MMOs. Different metal cations, including iron,[7–9] cobalt,[10,11] nickel,[12–14] copper,[15,16] and zinc,[17] have been exchanged for zeolites, typically ZSM-5 zeolite which has the MFI-type framework. When these catalysts are activated by an oxidant such as N_2O,[18–20] H_2O_2,[21,22] O_2,[23,24] or H_2O,[25] highly reactive O species able to selectively oxidize methane to methanol at low temperature (<200 °C) are formed on the metal active site.

To date, most of the efforts in methane hydroxylation by

metal-exchanged zeolites have been devoted to Fe- and Cu-exchanged zeolites, in which the active sites have been fully characterized by spectroscopic methods and supported by density functional theory (DFT) calculations to have structures of $[FeO]^{2+}$,[26–28] $[Cu_2(\mu\text{-}O)]^{2+}$,[29–32] and $[Cu_3(\mu\text{-}O)_3]^{2+}$.[32–34] Although these active species can activate methane at low temperature, the methanol formed on the metal centers must be extracted off-line using a solvent or steam because it cannot desorb on its own. Such an extraction method leads to a diluted methanol solution, which requires a high-cost separation. It has also been shown from DFT calculations that the energies required for desorbing methanol from $[Fe]^{2+}$, $[2Cu]^{2+}$, and $[Cu_3(\mu\text{-}O)_2]^{2+}$ centers in zeolites are approximately four times higher than those required for activating methane.[28,32] Thus, alternative metal active sites that enable both facile methane activation and solvent-free methanol desorption are highly desirable.

In the gas-phase reaction of methane hydroxylation,[35–37] bare NiO^+ demonstrates a 100% methanol selectivity,[35] which is much higher than that for bare FeO^+ and CuO^+ cations (41% and 60%, respectively).[36] Despite such a great potential of nickel, the number of studies on methane hydroxylation by Ni-exchanged zeolites is very limited. Only in 2014, Shan et al.[13] reported UV-vis spectra of O_2-activated Ni-ZSM-5 showing the appearance of 22,800 cm^{-1} absorption band, which is similar to the 22,700 cm^{-1} absorption band of O_2-activated Cu-ZSM-5 initially assigned to a bis(μ-oxo)dicopper,[15] but then revised to a mono(μ-oxo)dicopper on the basis of resonance Raman (rR) spectra analyses.[29] Accordingly, the active site in Ni-ZSM-5 has

This journal is © The Royal Society of Chemistry 2018

Catal. Sci. Technol., 2018, **00**, 1-10 | 1

been concluded to have a structure of mono(μ-oxo)dinickel [Ni$_2$(μ-O)]$^{2+}$,[13] although no rR spectra have been reported for confirmation. This Ni active site was reported to hydroxylate methane at low temperature (175 °C) with an activation energy of 19.9 kcal/mol,[13] which is slightly higher than that for [Cu$_2$(μ-O)]$^{2+}$-ZSM-5 (15.7 kcal/mol).[29] However, DFT calculations have shown that the [Ni$_2$(μ-O)]$^{2+}$ active site in a large cluster model of ZSM-5 zeolite[38] and a periodic structure of MOR zeolite[39] requires very high activation energies (45.7 and 35.2 kcal/mol, respectively) to abstract a H atom of methane, which make the reaction impossible to proceed at low temperature. Thus, such a dinuclear Ni species can be eliminated from the candidacy of active site in Ni-ZSM-5. Alternatively, we have previously suggested a [NiO]$^+$ active site, which hydroxylates methane with a rate-determining activation barrier of only 19.0 kcal/mol.[40] Although this value agrees very well with the experimental one (19.9 kcal/mol),[13] such a mononuclear Ni motif, to the best of our knowledge, has never been observed in any experimental works of metal-exchanged zeolites. In fact, Itoh and co-workers have shown that bis(μ-oxo)dinickel [Ni$^{III}_2$(μ-O)$_2$]$^{2+}$ complexes exhibit a remarkable reactivity toward the C–H bond cleavage of phenols,[41] 1,4-cyclohexadine,[41] and xanthene.[42]

In this study, we employed DFT+U method with a semilocal functional to calculate detailed reaction energy diagrams of methane hydroxylation over various motifs of Ni active sites, including [Ni^{IV}O]$^{2+}$, [Ni$^{II}_2$(μ-O)]$^{2+}$, [Ni$^{III}_2$(μ-O)$_2$]$^{2+}$, and [Ni^{II}Ni$^{III}_2$(μ-O)$_3$]$^{2+}$, in the periodic structure of ZSM-5 zeolite. A suitable U value for each Ni cation is explored and determined by referring to the ground state and Ni-atom spin densities predicted by a more accurate hybrid-functional in large cluster models. On the basis of agreement between the presently computed and the previously reported experimental[13] activation barriers, we suggest the most likely active site structures in methane hydroxylation by Ni-ZSM-5.

2. Computational Details

2.1 Periodic Structure and Large Cluster Models

The MFI framework of ZSM-5 zeolite is composed of units of SiO$_4$ tetrahedra (T) positioned at twelve distinct T sites and has a three-dimensional pore system with ten-membered-ring (10-MR) straight channels (5.3 × 5.6 Å) in the [010] direction intersected by 10-MR zigzag channels (5.1 × 5.5 Å) in the [100] direction.[43,44] One unit cell of the MFI framework retrieved from the zeolite database[43] was used for constructing the periodic structure. Optimized unit cell with lattice parameters of a = 20.406 Å, b = 20.142 Å, and c = 13.522 Å, which are in good agreement with the experimental values of a = 20.07 Å, b = 19.92 Å, and c = 13.42 Å,[44] were used for all calculations. Two Si atoms of the zeolite were replaced by two Al atoms, resulting in a negative charge of –2 and a Si/Al ratio of 47. This negative charge is compensated by the [Ni^{IV}O]$^{2+}$, [Ni$^{II}_2$(μ-O)]$^{2+}$, [Ni$^{III}_2$(μ-O)$_2$]$^{2+}$, and [Ni^{II}Ni$^{III}_2$(μ-O)$_3$]$^{2+}$ active species to construct neutral systems. As shown in Fig. 1, we selected the δ-type 6-MR (T11/T11), 10-MR (T3/T3), and 8-MR (T7/T12) sites of the
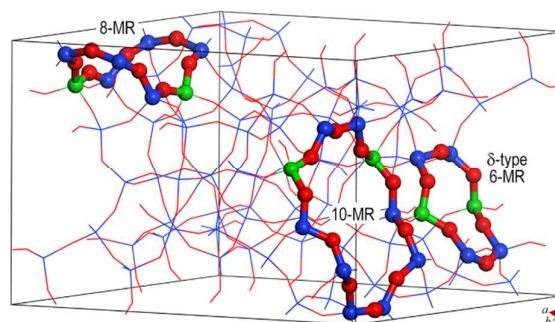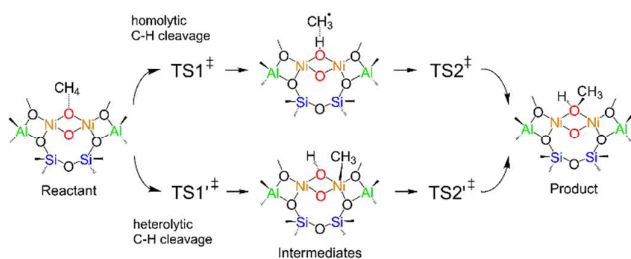

Fig. 1 Al pairs at the δ-type 6-MR (T11/T11), zigzag 10-MR(T3/T3), and 8-MR(T7/T12) sites of the MFI zeolite framework. The unit cell is depicted as a cube. Color legend: Si (blue), Al (green), and O (red)

zeolite as the Al-pair sites hosting the mono-, di-, and tri-nuclear Ni active species, respectively. These sites have been suggested by experiments[26,29,33] and DFT calculations[28,31,34] to host the square pyramidal [FeO]$^{2+}$, wide-angle [Cu$_2$(μ-O)]$^{2+}$, and circular [Cu$_3$(μ-O)$_3$]$^{2+}$, respectively, with the energetically most stable Al pair arrangements.

In addition to the periodic structures, hydrogen-terminated cluster models of [NiO]$^{2+}$-, [Ni]$^{2+}$-, [Ni$_2$(μ-O)]$^{2+}$-, [Ni$_2$]$^{2+}$-, [Ni$_2$(μ-O)$_2$]$^{2+}$, [Ni$_3$(μ-O)$_3$]$^{2+}$-, and [Ni$_3$(μ-O)$_2$]$^{2+}$-MFI zeolites were also calculated to provide good references of ground states and Ni-atom spin densities. As shown in Fig. S1 provided in the electronic supplementary information (ESI), the cluster models are constructed by 10 or 12 T (Si and Al) atoms, resulting in as large cluster models as those suggested by Woertink et al.[29] Same-size cluster models obtained from the optimized periodic structures were used for molecular orbital (MO) calculations.

2.2 Computational Methods

DFT calculations for the periodic structures were performed under the Kohn–Sham formulation[45,46] as implemented in the Vienna Ab–initio Simulation Package (VASP).[47,48] During calculations, all atoms were allowed to fully relax and the spin multiplicities were fixed. The Projector Augmented Wave (PAW) method was employed to describe the interaction between ion cores and electrons.[49,50] The electron exchange–correlation was treated by the generalized gradient approximation (GGA) based on the Perdew-Burke-Ernzerhof (PBE) functional.[51] To treat the strong correlation effects of Ni, a rotationally invariant GGA+U approach introduced by Dudarev et al.[52] was used with effective Hubbard parameters U$_{eff}$ being 0.0, 6.4, 4.0, and 3.0 eV, respectively for Ni^I, Ni^{II}, Ni^{III}, and Ni^{IV}, except for Ni^{II} in the reduced Ni^{2+}-MFI where U$_{eff}$ = 0.0 eV was used (for details, see Tables S1-S5 in ESI and a previous GGA+U study by Wang et al.[53]). The plane wave basis set with a cut-off energy of 550 eV was used for all calculations. Brillouin zone sampling was restricted to the Γ point only. The semiempirical Grimme's D2 method[54] was employed to account for van der Waals (vdW) dispersion correction. The conjugate gradient method was employed to optimize intermediate structures while the climbing-image Nudge

2 | *Catal. Sci. Technol.*, 2018, **00**, 1-10

This journal is © The Royal Society of Chemistry 2018

Scheme 1. Possible catalytic cycle of methane hydroxylation by $[Ni_2(\mu\text{-}O)_2]^{2+}$-zeolites

Scheme 2. Possible configurations of the outermost electrons in Ni^I, Ni^{II}, Ni^{III}, and Ni^{IV} cations, leading to the formation of doublet, singlet or triplet, quartet or doublet, and triplet or singlet states, respectively.

Elastic Band (CI-NEB) method[55,56] was used to locate transition states. Four NEB images generated using the Image-Dependent Pair Potentials (IDPP) method were used.[57] The geometry optimizations and CI-NEB calculations were considered to be converged when the maximum forces on all atoms were less than 0.05 eV/Å. Atomic spin densities were calculated using Bader analysis algorithm.[58,59] All optimized structures were visualized using VESTA.[60]

Spin-unrestricted DFT calculations for the large cluster models were performed by using the hybrid B3LYP functional[61–63] implemented in the Gaussian 09 program code. The choice of this functional, instead of other hybrid functionals such as PBE0,[64,65] is because the B3LYP functional can reasonably predict the ground state and Ni-atom spin densities of the studied active species, whereas the PBE0 functional in some cases fails to predict reasonable ground states (see Table S1). The vdW-D2 correction[54] was also taken into account. The 6-311+G* basis set[66,67] was used for the Ni atom, while the D95** basis set was used for the Si, Al, O, and H atoms. During the geometry optimizations, only the Al, Ni, O and H atoms were allowed to fully relaxed, while the Si atoms were fixed. For MO calculations, however, only the terminating H atoms were allowed to fully relaxed, while the remaining atoms were fixed to their optimized positions.

2.3 Reaction Mechanism and Spin States

Methane hydroxylation by metal-exchanged zeolites is a stepwise process involving three main steps: (1) oxidative activation of the catalyst by O_2, (2) main reaction of methane, and (3) methanol extraction using steam. Focusing on the second step, Scheme 1 shows two possible reaction mechanisms, namely homolytic and heterolytic H-atom abstraction (HAA) mechanisms, in which a respective methyl radical or methyl ligand is considered as a reaction intermediate separating the first and second halves of the reaction.[68] In both mechanisms, two transitions states corresponding to H–CH_3 bond cleavage (**TS1**) and HO–CH_3 rebound (**TS2**) are involved. However, while the rebound process in the homolytic HAA mechanism is usually barrierless (or very small activation barrier),[31,34] that in the heterolytic HAA mechanism requires a relatively high activation energy to cleave the Ni–CH_3 bond before the HO–CH_3 rebound takes place.[38,40] In this study, we considered only the homolytic HAA mechanism.

In methane hydroxylation over the $[Ni_2(\mu\text{-}O)_2]^{2+}$-MFI, for example, Ni^{III} and Ni^{II} are respectively involved in the first half
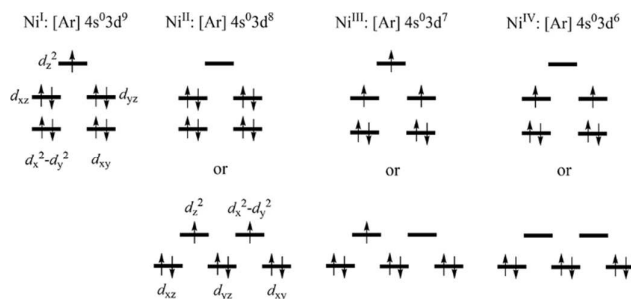
(i.e. reactant, **TS1**, and radical intermediate) and second half (i.e. **TS2** and product) of the reaction, which thus require the use of two distinct U_{eff} values of 4.0 and 6.4 eV, respectively. Consequently, the calculated total energies between the two halves of the reaction are incomparable. Thus, to estimate the relative energy between them, we refer to the energy difference between the $[Ni^{III}_2O_2]^{2+}$-MFI + CH_4 and $[Ni^{II}_2O]^{2+}$-MFI + CH_3OH cluster models calculated by using the B3LYP functional (Table S6). Moreover, such distinct U_{eff} values also make the CI-NEB calculations for locating **TS2** difficult to perform since the radical intermediate and product structures are optimized unequally. For this reason and another reason of **TS2** being less important than the rate-determining **TS1**, in this study we omitted **TS2** from calculations and assumed that the HO–CH_3 rebound is a barrierless process.

The Ni^I, Ni^{II}, Ni^{III}, and Ni^{IV} cations have electronic configurations of [Ar] $4s^0 3d^9$, [Ar] $4s^0 3d^8$, [Ar] $4s^0 3d^7$, and [Ar]
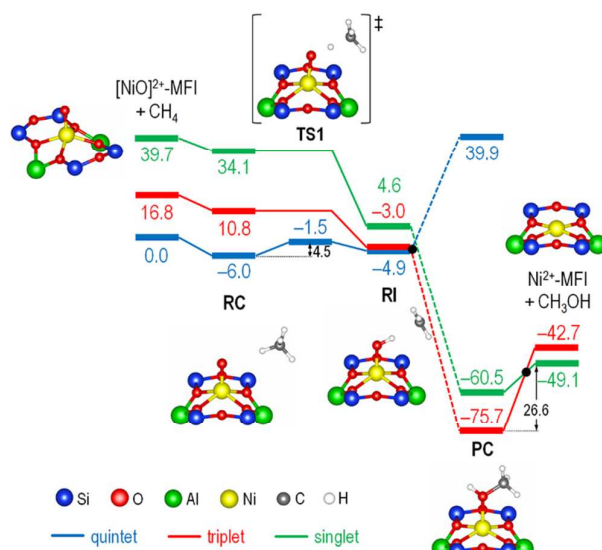
Fig. 2. Reaction energy diagrams and optimized ground-state structures of all intermediates in methane hydroxylation over $[NiO]^{2+}$-MFI. U_{eff} = 3.0 and 0.0 eV are used for calculating the first and second halves of the reaction, respectively. All energies are given in kcal/mol. Dashed lines indicate relative energies estimated from the cluster model calculations (Table S6). **RC**, **TS**, **RI**, and **PC** stand for reactant complex, transition state, radical intermediate, and product complex, respectively. Only the active site and zeolite ring are shown, while the remaining atoms of the zeolites are omitted for clarity.

$4s^0$ $3d^6$, respectively, where [Ar] refers to the argon-like core structure. As shown in Scheme 2, arranging these outermost electrons, we obtain some possible ways for filling the 3d orbitals of each Ni cation, which lead to various spin states. However, to avoid complexities with the U_{eff} values (see Table S1), in this study we considered only the most likely high-spin and low-spin states, as follow: quintet, triplet, and closed-shell singlet states for the reaction on the $[Ni^{IV}O]^{2+}$-MFI; quintet, (triplet), and open-shell singlet states for the reaction on the $[Ni^{II}_2(\mu\text{-}O)]^{2+}$-MFI; (quintet), triplet, and open-shell singlet states for the reaction on the $[Ni^{III}_2(\mu\text{-}O)_2]^{2+}$-MFI; septet, (quintet), and triplet states for the reaction on the $[Ni^{II}Ni^{III}_2(\mu\text{-}O)_3]^{2+}$-MFI. Values in the parentheses are additional spin states considered for the second half of the reaction.

3. Results and discussion

3.1 Methane Hydroxylation by $[NiO]^{2+}$-MFI

As shown in Fig. 2, the $[Ni^{IV}O]^{2+}$-MFI has a quintet ground state, where the Ni and O (oxo) atoms have spin densities of 1.95 and 1.46, respectively (Table 1). This indicates that the Ni^{IV} cation prefers the two unpaired electronic configuration (triplet state, Scheme 2), but an additional, strong radical character from the oxo atom stabilizes the quintet state to be the ground state. The reaction begins with the formation of reactant complex (**RC**), where methane is adsorbed on the active site with an adsorption energy being −6.0 kcal/mol. Subsequently, a C–H bond of methane is cleaved via a radical-like transition state (**TS1**) with an activation energy of $E_a^{TS1} = $ 4.5 kcal/mol to form a radical intermediate (**RI**). The calculated E_a^{TS1} is too small when compared to the experimental value (19.9 kcal/mol),[13] eliminating the possibility for $[NiO]^{2+}$ to be the actual active site in NI-ZSM-5. The separated C···H distance of **TS1** (1.324 Å, see Table 1) is found to be comparable with that for $[Cu_2(\mu\text{-}O)]^{2+}$-MOR (1.357 Å),[32] indicating similarly late transition states despite the fact that the two catalysts are totally different in the reactivity toward methane. The CI-NEB calculations for **TS1** in the triplet and closed-shell singlet states, on the other hand, do not result in a radical-like structure, but a full radical structure, suggesting that methane's C–H bond cleavage in these two spin states is a barrierless process.

Table 1. Geometrical Parameters and Atomic Spin Densities for All Intermediates in Methane Hydroxylation over $[NiO]^{2+}$-MFI.

	Ground state [a]	d_{Ni-O} (Å) [b]	d_{O-C} (Å) [b]	d_{C-H} (Å) [b]	d_{O-H} (Å) [b]	Atomic Spin Density		
						Ni	O	C
$[NiO]^{2+}$-MFI	Q	1.676	-	-	-	1.95	1.46	-
RC	Q	1.678	3.554	1.100	2.471	1.95	1.45	0.00
TS1	Q	1.758	2.574	1.324	1.251	1.90	1.08	0.50
RI	Q	1.780	2.910	1.897	1.013	1.91	0.71	0.86
PC	T	2.009	1.464	2.013	0.976	1.62	0.07	0.00
Ni^{2+}-MFI	CSS	-	-	-	-	0.00	0.00	0.00

[a] Q, T, and CSS stand for quintet, triplet, and closed-shell singlet states, respectively. [b] O and H correspond to the active O and abstracted H atoms, respectively.
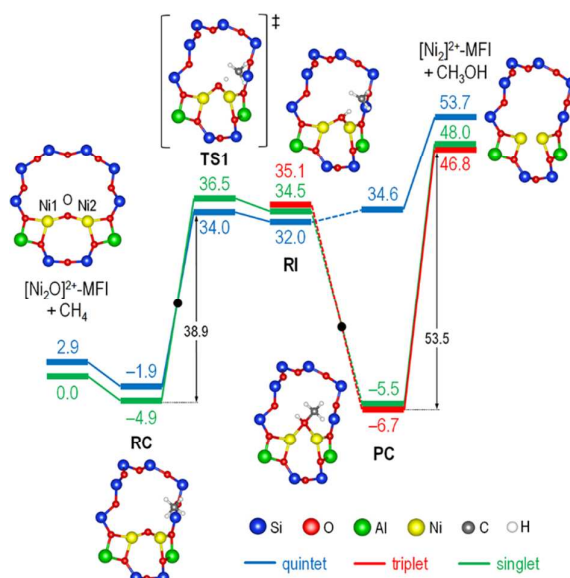

Fig. 3. Reaction energy diagrams and optimized ground-state structures of all intermediates in methane hydroxylation over $[Ni_2(\mu\text{-}O)]^{2+}$-MFI. U_{eff} = 6.4 and 0.0 eV are used for calculating the first and second halves of the reaction, respectively. All energies are given in kcal/mol. Structure notations are as in Fig. 2.

In the second half of the reaction, the OH moiety and CH$_3^•$ radical are directly rebound to form a product complex (**PC**) of methanol, expecting a spin inversion from the quintet to the triplet state. The formed methanol is then desorbed from the reduced Ni^{II} center with a desorption energy of E_{des}^{MeOH} = 26.6 kcal/mol. A spin inversion from the triplet to closed-shell singlet state is expected to occur in the exit channel of the reaction. Both calculations using the periodic structure and cluster model (B3LYP functional) presented in Table S1 show that Ni^{2+}-MFI has an unexpected ground state of closed-shell singlet state rather than the triplet state. This was also found in other square planar Ni complexes reported by Bachler et al.,[69] suggesting that the correlation effects of the Ni center in a square planar structure are weak and thus the DFT+U method is not necessary for the calculations. In the otherwise case, where U_{eff} = 6.4 eV is used, the triplet state is predicted as the ground state (Table S2).

3.2 Methane Hydroxylation by $[Ni_2(\mu\text{-}O)]^{2+}$-MFI

As shown in Fig. 3, the $[Ni^{II}_2(\mu\text{-}O)]^{2+}$-MFI prefers the open-shell singlet as the ground state, where the two unpaired electrons from one of the Ni^{II} centers are antiferromagnetically coupled with the two unpaired electrons from the other Ni^{II} center (see Ni-atom spin densities in Table 2). While **RC** is also formed in the open-shell singlet state with a methane adsorption energy of −4.9 kcal/mol, the subsequent C–H bond cleavage via **TS1** occurs in the quintet state with a very high activation energy of E_a^{TS1} = 38.9 kcal/mol. This value agrees very well with the previous theoretical result for $[Ni_2(\mu\text{-}O)]^{2+}$-MOR (35.2 kcal/mol),[39] but significantly differs from the experimentally measured activation barrier (19.9 kcal/mol).[13] In a similar case

4 | *Catal. Sci. Technol.*, 2018, **00**, 1-10

This journal is © The Royal Society of Chemistry 2018

of methane hydroxylation over $[Ni_2(\mu\text{-}O)]^{2+}$-MFI cluster model considering the heterolytic HAA mechanism, the methane activation barrier was reported to be low (14.1 kcal/mol), but the rate-determining step of the reaction with a higher activation barrier of 45.7 kcal/mol was found to be the HO–CH$_3$ rebound.[38] Thus, our results support the previous DFT work concluding that the mono(μ-oxo)dinickel $[Ni_2(\mu\text{-}O)]^{2+}$ is unlikely the active site.[38] Expecting a spin inversion to the quintet state, **TS1** is predicted to have a rather long C···H distance of 1.576 Å, which is quite similar to that for **RI** (1.851 Å), indicating a very late transition state that leads to a highly endothermic formation of **RI**.[70,71]

Table 2. Geometrical Parameters and Atomic Spin Densities for All Intermediates in Methane Hydroxylation over $[Ni_2(\mu\text{-}O)]^{2+}$-MFI. The atom labels are as on Fig. 3.

	Ground state [a]	d_{Ni-Ni} (Å) [b]	$\angle_{Ni-O-Ni}$ (°) [b]	d_{Ni-O} (Å) [b]	d_{O-C} (Å) [b]	d_{C-H} (Å) [b]	d_{O-H} (Å) [b]	Atomic Spin Density			
								Ni1	Ni2	O	C
$[Ni_2O]^{2+}$-MFI	OSS	3.291	143.4	1.733, 1.733	-	-	-	1.71	−1.71	0.00	-
RC	OSS	3.308	145.6	1.731, 1.731	3.518	1.098	2.432	1.71	−1.71	0.00	0.00
TS1	Q	3.075	114.7	1.826, 1.825	2.639	1.576	1.069	1.49	1.49	0.22	0.65
RI	Q	3.100	114.4	1.845, 1.843	1.006	1.851	1.005	1.44	1.44	0.15	0.83
PC	T	2.326	71.0	2.000, 2.003	1.495	2.032	0.979	0.94	0.95	0.02	0.00
$[Ni_2]^{2+}$-MFI	T	2.421	-	-	-	-	-	0.94	0.93	-	-

[a] Q, T, and OSS stand for quintet, triplet, and open-shell singlet states, respectively. [b] O and H correspond to the active O and abstracted H atoms, respectively.
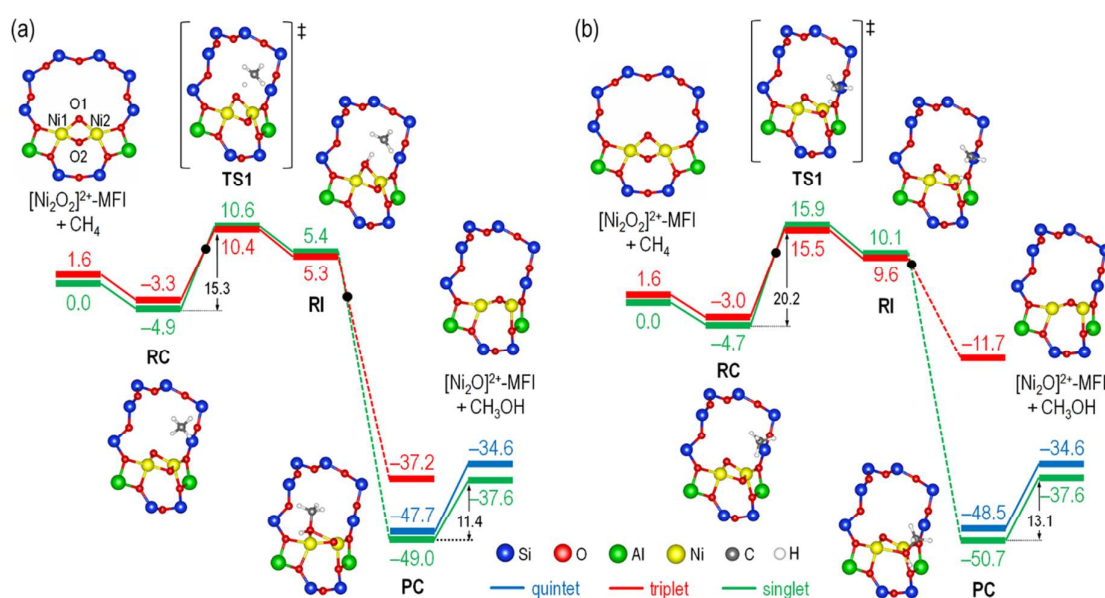

Fig. 4. Reaction energy diagrams and optimized ground-state structures of all intermediates in methane hydroxylation over $[Ni_2(\mu\text{-}O)_2]^{2+}$-MFI with the (a) O1 and (b) O2 atoms serving as the active O species. U$_{eff}$ = 4.0 and 6.4 eV are used for calculating the first and second halves of the reaction, respectively. All energies are given in kcal/mol. Structure notations are as in Fig. 2.

RI is expectedly formed in the quintet state rather than the open-shell singlet state, due to the instability of methyl radical in the singlet state. In the triplet state, on the other hand, our computational results show that each Ni atom of **RI** has a spin density of 1.43, forcing the C atom to have a negative spin density of −0.87 and thus resulting in an unstable CH$_3$• structure. A spin inversion is again expected to occur from the quintet to the triplet state during the recombination between the CH$_3$• radical and the OH moiety, forming **PC** of methanol that lies only 1.8 kcal/mol below **RC**, as expected from a rather unstable Ni^I cations formed in **PC**. **PC** in the quintet state is found to be highly unstable because each of the Ni^I cations has a spin density of 1.73 (two unpaired electrons), which forcefully changes the electronic configuration of Ni^I to [Ar] 4s^1 3d^8. The methanol desorption energy is calculated to be very

high (E_{des}^{MeOH} = 53.5 kcal/mol), as high as that for $[Cu_2(\mu\text{-}O)]^{2+}$-MOR (> 54 kcal/mol).[32]

3.3 Methane Hydroxylation by $[Ni_2(\mu\text{-}O)_2]^{2+}$-MFI

The $[Ni^{III}_2(\mu\text{-}O)_2]^{2+}$-MFI in the triplet state has two bridging O atoms that differ in spin density (Table S1), indicating that these atoms have distinct abilities to abstract the H atom of methane.[32,72] Fig. 4a shows energy diagrams of methane hydroxylation by $[Ni_2(\mu\text{-}O)_2]^{2+}$-MFI with the O1 atom serving as the H-atom abstracting species. Our calculations using the B3LYP and PBE functionals in the respective cluster model and periodic structure show that $[Ni_2(\mu\text{-}O)_2]^{2+}$-MFI prefers the open-shell singlet state, where the unpaired electron from one of the two Ni^{III} centers is antiferromagnetically coupled with the unpaired electron from the other Ni^{III} center (Table 3).

The adsorption of methane on the active site also takes place in the open-shell singlet state with an adsorption energy of −4.9 kcal/mol. The subsequent C–H bond cleavage of methane via **TS1** to form **RI** requires an activation energy of E_a^{TS1} = 15.3 kcal/mol, which agrees quite well with the experimental value (19.9 kcal/mol)[13] and the previous theoretical result for [Ni$_2$(μ-O)$_2$]$^{2+}$-MOR (17.8 kcal/mol).[39]

During the cleavage, a spin inversion is expected to occur in the vicinity of the crossing point. The separated C···H distance of **TS1** (1.283 Å) is found to be shorter than that for [Cu$_2$(μ-O)]$^{2+}$-MFI (1.391 Å),[31] indicating an early transition state which results in a less endothermic formation of **RI** (10.2 kcal/mol versus 14.6[31] kcal/mol). This is in accordance with the Hammond-Leffler postulate.[70,71]

Table 3. Geometrical Parameters and Atomic Spin Densities for All Intermediates in Methane Hydroxylation over [Ni$_2$(μ-O)$_2$]$^{2+}$-MFI. The atom labels are as on Fig. 4a.

	Ground state ^{a}	d_{Ni-Ni} (Å)	∠$_{Ni-O-Ni}$ (°) ^{b}	d_{Ni-O} (Å) ^{b}	d_{O-C} (Å) ^{b}	d_{C-H} (Å) ^{b}	d_{O-H} (Å) ^{b}	Atomic Spin Density				
								Ni1	Ni2	O1	O2	C
[Ni$_2$O$_2$]$^{2+}$-MFI	OSS	2.762	100.5, 101.5	1.796, 1.797, 1.783, 1.783	-	-	-	−1.02	1.02	−0.01	0.00	-
O1 atom serving as the H-atom abstracting agent												
RC	OSS	2.769	100.7	1.797, 1.798	3.604	1.097	2.516	−1.02	1.03	0.01	0.00	0.00
TS1	T	2.673	89.5	1.875, 1.922	2.550	1.283	1.273	0.76	0.13	0.38	0.20	0.42
RI	T	2.712	88.5	2.002, 1.884	2.856	1.868	1.007	0.06	0.76	0.08	0.19	0.84
PC	OSS	2.927	78.7	2.319, 2.295	1.475	2.014	0.977	−1.75	1.75	0.00	0.00	0.00
O2 atom serving as the H-atom abstracting agent												
RC	OSS	2.758	101.6	1.780, 1.780	3.447	1.097	2.401	−1.01	1.02	0.01	0.00	0.00
TS1	T	2.704	92.0	1.942, 1.817	2.568	1.299	1.274	0.09	0.99	−0.05	0.35	0.44
RI	T	2.746	91.2	1.971, 1.871	2.908	1.917	1.004	0.06	1.20	−0.24	−0.02	0.83
PC	OSS	2.869	77.2	2.283, 2.317	1.465	2.007	0.981	−1.73	1.73	0.00	0.00	0.00
[Ni$_2$O]$^{2+}$-MFI	OSS	3.267	141.0	1.733, 1.733	-	-	-	−1.71	1.71	0.00	-	-

^{a} T and OSS stand for triplet and open-shell singlet states, respectively. ^{b} O and H correspond to the active O and abstracted H atoms, respectively.

In the second half of the reaction, the CH$_3$$^\bullet$ radical of **RI** is recombined directly with the OH moiety to form a methanol molecule (**PC**), where the open-shell singlet is again preferred as the ground state and thus another spin inversion is expected to occur during the recombination. The methanol desorption energy is calculated to be low (E_{des}^{MeOH} = 11.4 kcal/mol), which is even lower than the E_a^{TS1} and much lower than that for [Ni$_2$(μ-O)]$^{2+}$-MFI (see section 3.2). This is primarily due to the high stability of two Ni^{II} centers formed on the reduced active site as well as the significantly elongated Ni–O1–Ni bond lengths to about 2.3 Å (Table 3). This suggests that the formed methanol can readily be desorbed from the active centers at the same temperature as that for methane activation, enabling the possibility of spontaneous, solvent-free, and on-line methanol desorption which can shorten the overall cycle times.

Fig. 4b shows energy diagrams for the reaction over the O2 atom of the [Ni$_2$(μ-O)$_2$]$^{2+}$ active site. The ground state and its changes along the reaction are similar to the previous case when the O1 atom served as the active species, but here the E_a^{TS1} = 20.2 kcal/mol is slightly higher, as also indicated by a slightly longer C···H distance of **TS1** (1.299 Å). Moreover, the E_{des}^{MeOH} = 13.1 kcal/mol is also found to be slightly higher, suggesting that methane hydroxylation on the O1 atom is energetically more favorable than that on the O2 atom.

Having good agreement of activation barrier, next we analyze the molecular orbitals of **RC** and **TS1** cluster models, where the O1 atom acts as the H-atom abstracting species. In the triplet state of [Ni$_2$(μ-O)$_2$]$^{2+}$-MFI, there are two singly occupied molecular orbitals (SOMOs) that are similar to those for [Cu$_2$(μ-O)]$^{2+}$-MFI in the same spin state.[29,31,68] The first

SOMO, SOMO(1), is a pair of occupied α-σ* and unoccupied β-σ* orbitals (Fig. 5, orange lines). The second SOMO, SOMO(2), on the other hand, is a pair of occupied α-π$_x$* and unoccupied β-π$_x$* orbitals (Fig. 5, blue lines). Since the unoccupied parts of these two SOMOs, i.e. β-σ* and β-π$_x$* orbitals, are lower in energy than the lowest unoccupied molecular orbital of the α-spin (α-LUMO, black line in Fig. 5), electrons from methane are more likely to be transferred here than to the α-LUMO.

Focusing on these two empty β-σ* (Ni d_{z^2} − O p_z) and β-π$_x$* (Ni d_{xz} − O p_x) orbitals, we found that the O1 p_z orbital of

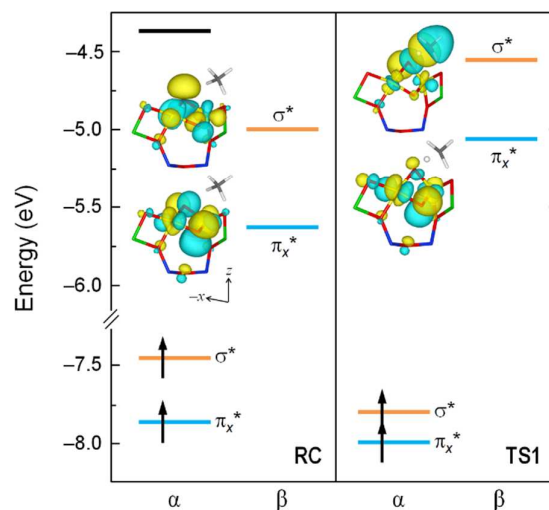**Fig. 5** Molecular orbitals of **RC** and **TS1** cluster models in methane hydroxylation over [Ni$_2$(μ-O)$_2$]$^{2+}$-MFI in the triplet state. Only selected orbitals are shown while the remaining orbitals are omitted for clarity. Orange, blue, and black lines correspond to SOMO(1), SOMO(2), and α-LUMO, respectively.
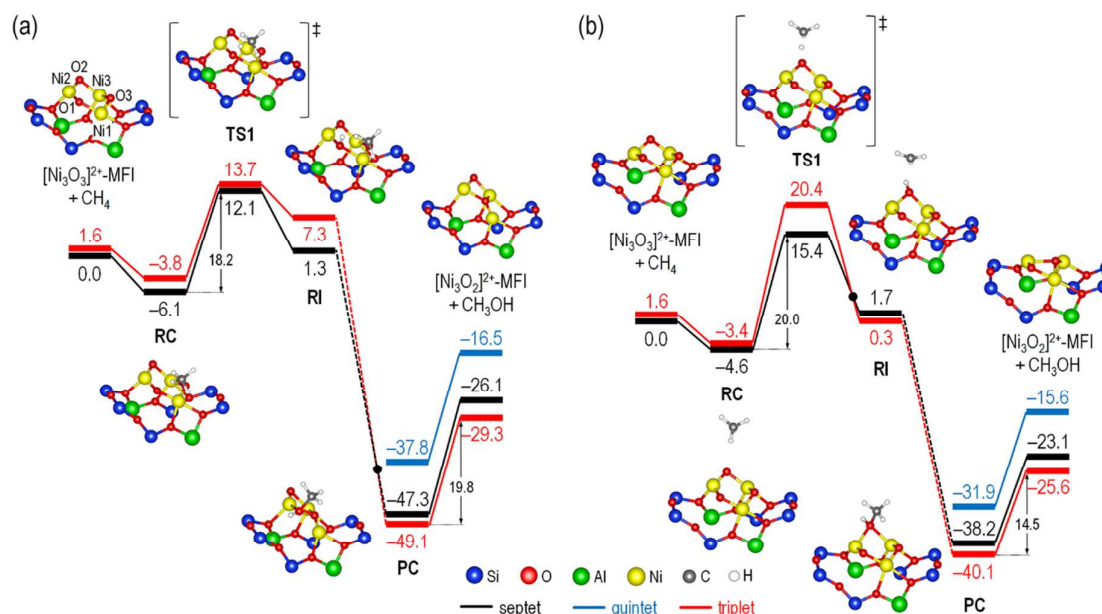
6 | *Catal. Sci. Technol.*, 2018, **00**, 1-10

This journal is © The Royal Society of Chemistry 2018

Fig. 6. Reaction energy diagrams and optimized ground-state structures of all intermediates and transition states in methane hydroxylation over $[Ni_3(\mu\text{-}O)_3]^{2+}$-MFI with the (a) O1 and (b) O2 atoms serving as the active O species. U_{eff} = 4.0 and 6.4 eV are used for calculating the first and second halves of the reaction, respectively. All energies are given in kcal/mol. Structure notations are as in Fig. 2.

the β-σ*, which initially directs to the z axis (perpendicular to the zeolite channel) and overlaps with the Ni d_{z^2} orbitals to form the Ni–$(\mu\text{-}O)_2$–Ni bonds, changes its direction toward methane as soon as the C–H bond of methane is cleaved. Moreover, it makes significant interactions with the CH₄-HOMO (highest occupied molecular orbital) located at −10.54 eV or higher due to zeolite confinement,[31,73] suggesting that the β-σ* is the acceptor orbital responsible for the H-atom abstraction of methane. In the β-π_x* orbital, on the other hand, the O1 p_x orbital initially lays down (parallel with the zeolite channel), but then directs to the z axis with a significantly smaller density. Such changes in the orbital direction and interaction are also reflected in the changes of SOMO energies, where the α-σ* and α-π_x* orbitals are stabilized to lower energies while the β-σ* and β-π_x* orbitals are destabilized to higher energies.

3.4 Methane Hydroxylation by $[Ni_3(\mu\text{-}O)_3]^{2+}$-MFI

In this reaction, U_{eff} = 4.0 eV is used for calculating the first half of the reaction despite the fact that the active species is a mix-valent $[Ni^{II}Ni^{III}_2(\mu\text{-}O)_3]^{2+}$ structure. However, the $[Ni_3(\mu\text{-}O)_3]^{2+}$ can actually be described as either $[Ni^{II}Ni^{III}_2(\mu\text{-}O)_3]^{2+}$, $[Ni^{I}Ni^{II}_2(\mu\text{-}O^\bullet)_3]^{2+}$, or $[Ni^{II}_3(\mu\text{-}O^\bullet)_2(\mu\text{-}O)]^{2+}$. According to the calculated Ni-atom and O-atom spin densities of the cluster model (Table S1), the preferred resonance structure is the $[Ni^{I}Ni^{II}_2(\mu\text{-}O^\bullet)_3]^{2+}$ in the septet ground state. Fig. 6 and Table 4 show that the use of U_{eff} = 4.0 in the periodic structure of $[Ni_3(\mu\text{-}O)_3]^{2+}$-MFI also predicts the septet state as the ground state and the $[Ni^{I}Ni^{II}_2(\mu\text{-}O^\bullet)_3]^{2+}$ as the preferred resonance structure, suggesting a good choice of U_{eff} value. Here, we evaluate two of the three bridging O atoms, i.e. O1 and O2 atoms, serving as the H-atom abstracting species. These two atoms have

different spin densities of 0.43 and 0.74, respectively, and thus different reactivities toward methane are expected. The O3 atom, on the other hand, is not evaluated for the reaction since reasonable **RC** and **RI** structures cannot be formed on it, due to a steric hindrance from the neighboring lattice.

Fig. 6a shows energy diagrams for the reaction over the O1 atom of the $[Ni_3(\mu\text{-}O)_3]^{2+}$ active site. The methane molecule is initially adsorbed on the active site with an adsorption energy of −6.1 kcal/mol, which is slightly stronger than the second case when the O2 atom serves as the active O species discussed below. This is due to the more constricted space resulting in stronger van der Waals forces that stabilize **RC**. The subsequent H-atom abstraction of methane via **TS1**, where the separated C⋯H distance is calculated to be 1.295 Å, requires an activation energy of E_a^{TS1} = 18.2 kcal/mol. This value is lower than the previous DFT result for $[Ni_3(\mu\text{-}O)_3]^{2+}$-MOR (25.6 kcal/mol),[39] but agrees quite well with the experimental value (19.9 kcal/mol).[13] The formed methyl radical still prefers the septet state before it recombines with the OH moiety to form **PC** in the open-shell triplet state, where the Ni2 and Ni3 atoms are coupled antiferromagnetically (Table 4). A desorption energy of E_{des}^{MeOH} = 19.8 kcal/mol, which is as low as the methane activation energy, is required to detach the formed methanol molecule from the active site. Such a low desorption energy is attributed mainly to the loosely bound methanol to the Ni centers with significantly elongated Ni1–O1–Ni2 bond lengths to more than 2.3 Å and to the high stability of three Ni^{II} centers formed on the reduced active site $[Ni^{II}_3(\mu\text{-}O)_2]^{2+}$.

Fig. 6b shows energy diagrams for methane hydroxylation over the $[Ni_3(\mu\text{-}O)_3]^{2+}$ active site with the O2 atom serving as the active O atom. In this case, the O2 atom is exposed to a larger space of zeolite cage, which causes a slightly weaker methane adsorption energy (−4.6 kcal/mol), as compared to

This journal is © The Royal Society of Chemistry 2018

Catal. Sci. Technol., 2018, **00**, 1-10 | **7**

the first case when the O1 atom served as the active O species. Also, the methane's C–H bond activation barrier (E_a^{TS1} = 20.2 kcal/mol) is found to be higher despite the higher spin density of the O2 atom and the shorter C···H distance of **TS1** (1.254 Å, Table 4). This is possibly because the O2 atom is located next to the neighboring lattice, which hinder and drive the radical-like species to an unfavorable location above the O1 atom (not in front of it), where the larger, freer space is located, and

eventually results in a destabilization of **TS1**. We also found that the calculated E_a^{TS1} is higher than that for $[Cu_3(\mu\text{-}O)_3]^{2+}$-MFI (12.9 kcal/mol, the O2 atom acts as the active species).[34] Unlike in the first case, here the spin inversion from the septet to the open-shell triplet state occurs before the formation of **RI**. Having a higher E_a^{TS1} and a less stable **PC** structure, methane hydroxylation on the O2 atom is energetically less favorable than that on the O1 atom.

Table 4. Geometrical Parameters and Atomic Spin Densities for All Intermediates in Methane Hydroxylation over $[Ni_3(\mu\text{-}O)_3]^{2+}$-MFI. The atom labels are as on Fig. 6a.

	Ground state [a]	$\angle_{Ni-O-Ni}$ (°) [b]	d_{Ni-O} (Å) [b]	d_{O-C} (Å) [b]	d_{C-H} (Å) [b]	d_{O-H} (Å) [b]	Atomic Spin Density						
							Ni1	Ni2	Ni3	O1	O2	O3	C
$[Ni_3O_3]^{2+}$-MFI	Sp	122.7, 96.1, 120.8	1.767, 1.736, 1.733, 1.850, 1.866, 1.707	-	-	-	0.76	1.68	1.69	0.43	0.74	0.47	-
O1 atom serving as the H-atom abstracting agent													
RC	Sp	124.9	1.768, 1.735	3.489	1.099	2.403	0.76	1.68	1.69	0.43	0.73	0.46	0.00
TS1	Sp	110.8	1.930, 1.840	2.537	1.295	1.270	1.62	1.62	0.99	0.61	0.20	0.24	0.42
RI	Sp	112.8	1.984, 1.872	3.052	2.423	0.977	1.67	1.62	0.97	0.18	0.16	0.27	0.88
PC	OST	82.6	2.340, 2.294	1.471	2.009	0.981	1.70	1.68	−1.68	0.02	0.03	0.19	0.00
O2 atom serving as the H-atom abstracting agent													
$[Ni_3O_2]^{2+}$-MFI	OST	-	-	-	-	-	1.70	−1.65	1.70	-	0.19	−0.04	-
RC	Sp	96.8	1.732, 1.846	3.293	1.096	2.259	0.76	1.68	1.70	0.43	0.73	0.47	0.00
TS1	Sp	97.9	1.800, 1.864	2.550	1.254	1.303	0.85	1.60	1.65	0.35	0.54	0.39	0.36
RI	OST	96.3	1.895, 1.886	2.920	2.013	0.989	0.89	−1.58	1.65	−0.33	0.05	0.33	0.87
PC	OST	87.5	2.147, 2.122	1.498	2.046	0.979	1.72	−1.57	1.68	−0.25	0.00	0.29	0.00
$[Ni_3O_2]^{2+}$-MFI	OST	-	-	-	-	-	1.74	−1.62	1.65	−0.09	-	0.20	-

[a] Sp and OST stand for septet and open-shell triplet states, respectively. [b] O and H correspond to the active O and abstracted H atoms, respectively.

In Fig. 7, we show the MOs of **RC** and **TS1** cluster models, where the O1 atom acts as the H-atom abstracting species. According to the report by Vogiatzis et al.,[74] there are two antibonding σ*, two bonding σ, and one nonbonding δ orbitals in the frontier orbitals of $[Cu_3(\mu\text{-}O)_3]^{2+}$-MOR in the doublet state. Similarly, in the septet state of $[Ni_3(\mu\text{-}O)_3]^{2+}$-MFI we found two σ* orbitals, namely an unoccupied σ_y^* and a singly occupied σ_x^* (black and orange lines, respectively, in Fig. 7

RC), while the remaining singly occupied orbitals (blue lines in Fig. 7 **RC**) involve two σ, one δ, one π*, and one π orbitals.

We are particularly interested in the empty, low-energy α-σ_y^* (Ni d_{xy} – O p_y), β-π* (Ni d_{xz} – O p_z), and β-π (Ni d_{xz} + O p_z) orbitals which potentially accept electrons from methane. Initially, the O1 and O3 p_y orbitals of the α-σ_y^* are parallel with the zeolite ring surface (y axis) and point toward the Ni1 d_{yz} orbital to make antibonding interactions involved in the O1–Ni1–O3 bonds. On the contrary, the O3 p_z orbitals of the β-π* and β-π are perpendicular to the zeolite ring surface and respectively make antibonding and bonding interactions resulting in a Ni3–O3 bond. However, after the H-atom abstraction of methane (Fig.7, **TS1**), only the O1 p_y orbital of the α-σ_y^* changes its direction toward methane and interacts with the CH$_4$-HOMO. This is mainly due to the involvement of the α-σ_y^* orbital in the Ni1–O1 bonds,[75] which cannot be found in the β-π* and β-π orbitals that are actually lower in energy. This renders α-σ_y^* suitable as the acceptor orbital responsible for the H-atom abstraction of methane. Such interactions between the donor and acceptor orbitals result in destabilizations of all α-spin and β-spin SOMOs to higher energies while the empty α-σ_y^* orbital is stabilized from −4.02 eV (**RC**) to −4.56 eV (**TS1**).
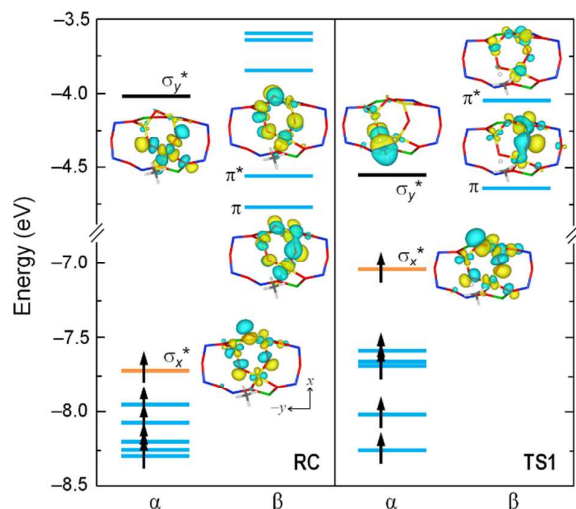

Fig. 7 Molecular orbitals of **RC** and **TS1** cluster models in methane hydroxylation over $[Ni_3(\mu\text{-}O)_3]^{2+}$-MFI in the septet state. Only selected orbitals are shown while the remaining orbitals are omitted for clarity. Black, orange, and blue lines correspond to the acceptor α-LUMO, singly occupied α-HOMO, and remaining SOMOs, respectively.

4. Conclusions

Using DFT+U method with the PBE functional, we have explored the hydroxylation of methane to methanol on various motifs of Ni active site, including $[NiO]^{2+}$, $[Ni_2(\mu\text{-}O)]^{2+}$, $[Ni_2(\mu\text{-}$

8 | *Catal. Sci. Technol.*, 2018, **00**, 1-10

This journal is © The Royal Society of Chemistry 2018

O)$_2$]$^{2+}$, and [Ni$_3$(μ-O)$_3$]$^{2+}$, in the periodic structure of ZSM-5 zeolite. While the [NiO]$^{2+}$- and [Ni$_2$(μ-O)]$^{2+}$-ZSM-5 are found to be so reactive and unreactive, respectively, that they might not be observed in experiments, the [Ni$_2$(μ-O)$_2$]$^{2+}$- and [Ni$_3$(μ-O)$_3$]$^{2+}$-ZSM-5 require reasonably low activation energies to cleave a C–H bond of methane (15.3 and 18.2 kcal/mol, respectively). More importantly, these values agree very well with the experimental value (19.9 kcal/mol).[13] Thus, we suggest these two active site motifs as possible candidates for the actual active site structure in methane hydroxylation by Ni-ZSM-5, in addition to the [NiO]$^{+}$-ZSM-5 previously suggested by our group.[40] Not only requiring a low methane activation barrier, the [Ni$_2$(μ-O)$_2$]$^{2+}$- and [Ni$_3$(μ-O)$_3$]$^{2+}$-ZSM-5 are also easy to desorb the formed methanol from the metal centers, as the required desorption energies are only 11.4 and 19.8 kcal/mol, respectively, much lower than that for [Cu$_2$(μ-O)]$^{2+}$-MOR (54-60 kcal/mol).[32] This may enable spontaneous, solvent-free, and on-line methanol desorption. Such remarkable features of [Ni$_2$(μ-O)$_2$]$^{2+}$- and [Ni$_3$(μ-O)$_3$]$^{2+}$-ZSM-5 will open up a new hope for metal-exchanged zeolites toward the low-temperature methane hydroxylation with high-selectivity and undiluted methanol. The present work can hopefully trigger more experimental studies especially on the spectroscopic and kinetic analyses of methane hydroxylation by Ni-ZSM-5 to confirm the present DFT predictions.

Conflicts of interest

There are no conflicts to declare.

Acknowledgements

References

1   A. C. Rosenzweig, C. A. Frederick, S. J. Lippard and P. Nordlund, *Nature*, 1993, **366**, 537–543.

2   A. C. Rosenzweig and S. J. Lippard, *Acc. Chem. Res.*, 1994, **27**, 229–236.

3   A. C. Rosenzweig, P. Nordlund, P. M. Takahara, C. A. Frederick and S. J. Lippard, *Chem. Biol.*, 1995, **2**, 409–418.

4   R. L. Lieberman and A. C. Rosenzweig, *Nature*, 2005, **434**, 177–182.

5   R. Balasubramanian, S. M. Smith, S. Rawat, L. A. Yatsunyk, T. L. Stemmler and A. C. Rosenzweig, *Nature*, 2010, **465**, 115–119.

6   S. I. Chan, K. H.-C. Chen, S. S.-F. Yu, C.-L. Chen and S. S.-J. Kuo, *Biochemistry*, 2004, **43**, 4421–4430.

7   V. I. Sobolev, K. A. Dubkov, O. V. Panna and G. I. Panov, *Catal. Today*, 1995, **24**, 251–252.

8   K. A. Dubkov, V. I. Sobolev, E. P. Talsi, M. A. Rodkin, N. H. Watkins, A. A. Shteinman and G. I. Panov, *J. Mol. Catal. A Chem.*, 1997, **123**, 155–161.

9   G. I. Panov, E. V. Starokon, M. V. Parfenov and L. V. Pirutko, *ACS Catal.*, 2016, **6**, 3875–3879.

10   N. V. Beznis, B. M. Weckhuysen and J. H. Bitter, *Catal. Lett.*, 2010, **136**, 52–56.

11   N. V. Beznis, A. N. C. van Laak, B. M. Weckhuysen and J. H. Bitter, *Microporous Mesoporous Mater.*, 2011, **138**, 176–183.

12   A. N. Mlinar, G. B. Baur, G. G. Bong, A. B. Getsoian and A. T. Bell, *J. Catal.*, 2012, **296**, 156–164.

13   J. Shan, W. Huang, L. Nguyen, Y. Yu, S. Zhang, Y. Li, A. I. Frenkel and F. Tao, *Langmuir*, 2014, **30**, 8558–8569.

14   Z.-P. Hu, C.-C. Weng, C. Chen and Z.-Y. Yuan, *Appl. Catal. A Gen.*, 2018, **562**, 49–57.

15   M. H. Groothaert, P. J. Smeets, B. F. Sels, P. A. Jacobs and R. A. Schoonheydt, *J. Am. Chem. Soc.*, 2005, **127**, 1394–1395.

16   P. J. Smeets, M. H. Groothaert and R. A. Schoonheydt, *Catal. Today*, 2005, **110**, 303–309.

17   J. Xu, A. Zheng, X. Wang, G. Qi, J. Su, J. Du, Z. Gan, J. Wu, W. Wang and F. Deng, *Chem. Sci.*, 2012, **3**, 2932.

18   E. V. Kondratenko and J. Pérez-Ramírez, *J. Phys. Chem. B*, 2006, **110**, 22586–22595.

19   G. Li, E. A. Pidko, I. A. W. Filot, R. A. van Santen, C. Li and E. J. M. Hensen, *J. Catal.*, 2013, **308**, 386–397.

20   M.-L. Tsai, R. G. Hadt, P. Vanelderen, B. F. Sels, R. A. Schoonheydt and E. I. Solomon, *J. Am. Chem. Soc.*, 2014, **136**, 3522–3529.

21   C. Hammond, M. M. Forde, M. H. Ab Rahim, A. Thetford, Q. He, R. L. Jenkins, N. Dimitratos, J. A. Lopez-Sanchez, N. F. Dummer, D. M. Murphy, A. F. Carley, S. H. Taylor, D. J. Willock, E. E. Stangland, J. Kang, H. Hagen, C. J. Kiely and G. J. Hutchings, *Angew. Chem. Int. Ed.*, 2012, **51**, 5129–5133.

22   Á. Szécsényi, G. Li, J. Gascon and E. A. Pidko, *ACS Catal.*, 2018, **8**, 7961–7972.

23   P. J. Smeets, R. G. Hadt, J. S. Woertink, P. Vanelderen, R. A. Schoonheydt, B. F. Sels and E. I. Solomon, *J. Am. Chem. Soc.*, 2010, **132**, 14736–14738.

24   M. H. Mahyuddin, T. Tanaka, A. Staykov, Y. Shiota and K. Yoshizawa, *Inorg. Chem.*, 2018, **57**, 10146–10152.

25   V. L. Sushkevich, D. Palagin, M. Ranocchiari and J. A. van Bokhoven, *Science*, 2017, **356**, 523–527.

26   B. E. R. Snyder, P. Vanelderen, M. L. Bols, S. D. Hallaert, L. H. Böttger, L. Ungur, K. Pierloot, R. A. Schoonheydt, B. F. Sels and E. I. Solomon, *Nature*, 2016, **536**, 317–321.

27   B. E. R. Snyder, L. H. Böttger, M. L. Bols, J. J. Yan, H. M. Rhoda, A. B. Jacobs, M. Y. Hu, J. Zhao, E. E. Alp, B. Hedman, K. O. Hodgson, R. A. Schoonheydt, B. F. Sels and E. I. Solomon, *Proc. Natl. Acad. Sci. U. S. A.*, 2018, 201721717.

28   M. H. Mahyuddin, Y. Shiota, A. Staykov and K. Yoshizawa, *Inorg. Chem.*, 2017, **56**, 10370–10380.

29   J. S. Woertink, P. J. Smeets, M. H. Groothaert, M. A. Vance, B. F. Sels, R. A. Schoonheydt and E. I. Solomon, *Proc. Natl. Acad. Sci. U. S. A.*, 2009, **106**, 18908–18913.

30   P. Vanelderen, B. E. R. Snyder, M.-L. Tsai, R. G. Hadt, J.

Vancauwenbergh, O. Coussens, R. A. Schoonheydt, B. F. Sels and E. I. Solomon, *J. Am. Chem. Soc.*, 2015, **137**, 6383–6392.

31 M. H. Mahyuddin, A. Staykov, Y. Shiota, M. Miyanishi and K. Yoshizawa, *ACS Catal.*, 2017, **7**, 3741–3751.

32 M. H. Mahyuddin, T. Tanaka, Y. Shiota, A. Staykov and K. Yoshizawa, *ACS Catal.*, 2018, **8**, 1500–1509.

33 S. Grundner, M. A. C. Markovits, G. Li, M. Tromp, E. A. Pidko, E. J. M. Hensen, A. Jentys, M. Sanchez-Sanchez and J. A. Lercher, *Nat. Commun.*, 2015, **6**, 7546.

34 G. Li, P. Vassilev, M. Sanchez-Sanchez, J. A. Lercher, E. J. M. Hensen and E. A. Pidko, *J. Catal.*, 2016, **338**, 305–312.

35 D. Schröder and H. Schwarz, *Angew. Chem. Int. Ed.*, 1995, **34**, 1973–1995.

36 N. Dietl, C. van der Linde, M. Schlangen, M. K. Beyer and H. Schwarz, *Angew. Chem. Int. Ed.*, 2011, **50**, 4966–4969.

37 Y. Shiota and K. Yoshizawa, *J. Am. Chem. Soc.*, 2000, **122**, 12317–12326.

38 A. A. Arvidsson, V. P. Zhdanov, P.-A. Carlsson, H. Grönbeck and A. Hellman, *Catal. Sci. Technol.*, 2017, **7**, 1470–1477.

39 A. R. Kulkarni, Z.-J. Zhao, S. Siahrostami, J. K. Nørskov and F. Studt, *Catal. Sci. Technol.*, 2018, **8**, 114–123.

40 M. H. Mahyuddin, A. Staykov, Y. Shiota and K. Yoshizawa, *ACS Catal.*, 2016, **6**, 8321–8331.

41 S. Itoh, H. Bandoh, M. Nakagawa, S. Nagatomo, T. Kitagawa, K. D. Karlin and S. Fukuzumi, *J. Am. Chem. Soc.*, 2001, **123**, 11168–11178.

42 Y. Morimoto, Y. Takagi, T. Saito, T. Ohta, T. Ogura, N. Tohnai, M. Nakano and S. Itoh, *Angew. Chem.*, 2018, **130**, 7766–7769.

43 C. Baerlocher and L. B. McCusker, Database of Zeolite Structures., http://www.iza-structure.org/databases/, (accessed 26 July 2018).

44 D. H. Olson, G. T. Kokotailo, S. L. Lawton and W. M. Meier, *J. Phys. Chem.*, 1981, **85**, 2238–2243.

45 P. Hohenberg and W. Kohn, *Phys. Rev.*, 1964, **136**, B864–B871.

46 W. Kohn and L. J. Sham, *Phys. Rev.*, 1965, **140**, A1133–A1138.

47 G. Kresse and J. Furthmüller, *Comput. Mater. Sci.*, 1996, **6**, 15–50.

48 G. Kresse and J. Furthmüller, *Phys. Rev. B: Condens. Matter Mater. Phys.*, 1996, **54**, 11169–11186.

49 P. E. Blöchl, *Phys. Rev. B: Condens. Matter Mater. Phys.*, 1994, **50**, 17953–17979.

50 G. Kresse and D. Joubert, *Phys. Rev. B: Condens. Matter Mater. Phys.*, 1999, **59**, 1758–1775.

51 J. P. Perdew, K. Burke and M. Ernzerhof, *Phys. Rev. Lett.*, 1996, **77**, 3865–3868.

52 S. L. Dudarev, G. A. Botton, S. Y. Savrasov, C. J. Humphreys and A. P. Sutton, *Phys. Rev. B: Condens. Matter Mater. Phys.*, 1998, **57**, 1505–1509.

53 L. Wang, T. Maxisch and G. Ceder, *Phys. Rev. B: Condens. Matter Mater. Phys.*, 2006, **73**, 195107.

54 S. Grimme, *J. Comput. Chem.*, 2006, **27**, 1787–1799.

55 G. Henkelman, B. P. Uberuaga and H. Jónsson, *J. Chem. Phys.*, 2000, **113**, 9901–9904.

56 G. Henkelman and H. Jónsson, *J. Chem. Phys.*, 2000, **113**, 9978–9985.

57 S. Smidstrup, A. Pedersen, K. Stokbro and H. Jónsson, *J. Chem. Phys.*, 2014, **140**, 214106.

58 G. Henkelman, A. Arnaldsson and H. Jónsson, *Comput. Mater. Sci.*, 2006, **36**, 354–360.

59 E. Sanville, S. D. Kenny, R. Smith and G. Henkelman, *J. Comput. Chem.*, 2007, **28**, 899–908.

60 K. Momma and F. Izumi, *J. Appl. Crystallogr.*, 2011, **44**, 1272–1276.

61 A. D. Becke, *Phys. Rev. A: At. Mol. Opt. Phys.*, 1988, **38**, 3098–3100.

62 C. Lee, W. Yang and R. G. Parr, *Phys. Rev. B: Condens. Matter Mater. Phys.*, 1988, **37**, 785–789.

63 S. H. Vosko, L. Wilk and M. Nusair, *Can. J. Phys.*, 1980, **58**, 1200–1211.

64 M. Ernzerhof and G. E. Scuseria, *J. Chem. Phys.*, 1999, **110**, 5029.

65 C. Adamo and V. Barone, *J. Chem. Phys.*, 1999, **110**, 6158.

66 A. J. H. Wachters, *J. Chem. Phys.*, 1970, **52**, 1033–1036.

67 P. J. Hay, *J. Chem. Phys.*, 1977, **66**, 4377–4384.

68 M. H. Mahyuddin, Y. Shiota, A. Staykov and K. Yoshizawa, *Acc. Chem. Res.*, 2018, **51**, doi: 10.1021/acs.accounts.8b00236.

69 V. Bachler, G. Olbrich, F. Neese and K. Wieghardt, *Inorg. Chem.*, 2002, **41**, 4179–4193.

70 G. S. Hammond, *J. Am. Chem. Soc.*, 1955, **77**, 334–338.

71 J. E. Leffler, *Science*, 1953, **117**, 340–341.

72 N. Dietl, M. Schlangen and H. Schwarz, *Angew. Chem. Int. Ed.*, 2012, **51**, 5544–5555.

73 A. Corma, G. Hermenegildo, G. Sastre and P. M. Viruela, *J. Phys. Chem. B*, 1997, **101**, 4575–4582.

74 K. D. Vogiatzis, G. Li, E. J. M. Hensen, L. Gagliardi and E. A. Pidko, *J. Phys. Chem. C*, 2017, **121**, 22295–22302.

75 A. Rosa, G. Ricciardi and E. J. Baerends, *Inorg. Chem.*, 2010, **49**, 3866–3880.

10 | *Catal. Sci. Technol.*, 2018, **00**, 1-10

This journal is © The Royal Society of Chemistry 2018

Graphical abstract

DFT calculations suggest $[Ni_2(\mu\text{-}O)_2]^{2+}$ and $[Ni_3(\mu\text{-}O)_3]^{2+}$ species as two possible active sites in methane hydroxylation by Ni-ZSM-5 zeolite. Both of them are predicted to activate methane and desorbed the formed methanol with low activation and desorption energies.